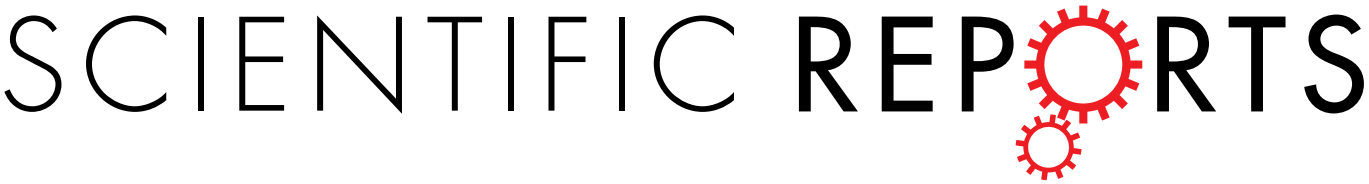

OPEN

Interfacial structures and energetics of the strengthening precipitate phase in creep-resistant Mg-Nd-based alloys

Received: 23 August 2016
Accepted: 07 December 2016
Published: 17 January 2017

D. Choudhuri, R. Banerjee & S. G. Srinivasan

The extraordinary creep-resistance of Mg-Nd-based alloys can be correlated to the formation of *nanoscale-platelets* of β_1-Mg_3Nd precipitates, that grow along $\langle 11\bar{2}0\rangle_{Mg}$ in bulk *hcp*-Mg and on dislocation lines. The growth kinetics of β_1 is sluggish even at high temperatures, and presumably occurs via vacancy migration. However, the rationale for the high-temperature stability of precipitate-matrix interfaces and observed growth direction is unknown, and may likely be related to the interfacial structure and excess energy. Therefore, we study two interfaces– $\{112\}_{\beta 1}/\{\bar{1}100\}_{Mg}$ and $\{111\}_{\beta 1}/\{11\bar{2}0\}_{Mg}$– that are commensurate with β_1/*hcp*-Mg orientation relationship via first principles calculations. We find that β_1 acquires plate-like morphology to reduce small lattice strain via the formation of energetically favorable $\{112\}_{\beta 1}/\{\bar{1}100\}_{Mg}$ interfaces, and predict that β_1 grows along $\langle 11\bar{2}0\rangle_{Mg}$ on dislocation lines due to the migration of metastable $\{111\}_{\beta 1}/\{11\bar{2}0\}_{Mg}$. Furthermore, electronic charge distribution of the two interfaces studied here indicated that interfacial-energy of coherent precipitates is sensitive to the population of distorted lattice sites, and their spatial extent in the vicinity of interfaces. Our results have implications for alloy design as they suggest that formation of β_1-like precipitates in the *hcp*-Mg matrix will require well-bonded coherent interface along precipitate broad-faces, while simultaneously destabilizing other interfaces.

Magnesium (Mg) alloys have tremendous potential as structural materials for automotive applications in engine block, transmission parts due to their lightweight. The concomitant fuel savings is however, thwarted by their unfavorable creep strength[1–4]. Mg-rare earth (RE) alloys are exceptions with demonstrated excellent creep resistance[1–3]. Their superior creep properties are correlated to the formation of high volume fractions of strengthening precipitates based on RE intermetallic compounds[4,5]. However, the scarcity and high cost of RE elements limits the development of creep–resistant Mg-RE alloys. This work is motivated by gaining an atomistic understanding of commonly found strengthening precipitates in creep-resistant Mg-RE alloys, and inform Mg-alloy design approaches by providing energetics and bonding characteristics associated with their presence within the *hcp*-Mg matrix. Therefore, we have investigated the structure of interface between intermetallic precipitate phase β_1 (an ordered cubic structure) and *hcp*-Mg. This precipitate typically forms in Mg-Nd-based alloys like Mg-Nd, Mg-Nd-Y and Mg-Nd-Y-Zr, e.g. commercial WE43 and WE54 [5–7]. The coherent β_1 phase has a plate-like morphology, and shares an $(0001)_{Mg}//(011)_{\beta 1}$, $[\bar{1}100]_{Mg}//[21\bar{1}]_{\beta 1}$ and $[11\bar{2}0]_{Mg}//[1\bar{1}1]_{\beta 1}$ orientation relationship (OR) with *hcp*-Mg[5–12]. TEM results also indicate that plate-like β_1 precipitates always forms with a high aspect ratio, and its broad-face $\{21\bar{1}\}_{\beta 1}$ parallel to $\{\bar{1}100\}_{Mg}$[4–11]. Furthermore, β_1 nucleating within the Mg-matrix is associated with the orthorhombic β' precipitate phase[5,7], or as self-accommodating β_1 triads[5,11], and heterogeneously along dislocation lines via accommodation of β_1 stress-free transformation strains associated with β_1 formation[7–9,13,14]. Heterogeneous formation is particularly useful in restraining high-temperature creep deformation, because its dynamic nucleation arrests dislocation movement and enhances the creep-resistance of Mg-RE alloys[4,9–11].

The formation tendencies of β_1 precipitates have been characterized experimentally[5–11], and its evolution within Mg matrix and on dislocations studied via phase-field models[12–14]. Despite extensive studies on β_1 phase, basic thermodynamic quantities like β_1/Mg interfacial energies are yet to be determined unequivocally.

Department of Materials Science and Engineering, University of North Texas, Denton, TX, 76191, USA. Correspondence and requests for materials should be addressed to D.C. (email: deep.choudhuri@gmail.com) or R.B. (email: Raj.Banerjee@unt.edu) or S.G.S. (email: Srinivasan.Srivilliputhur@unt.edu)

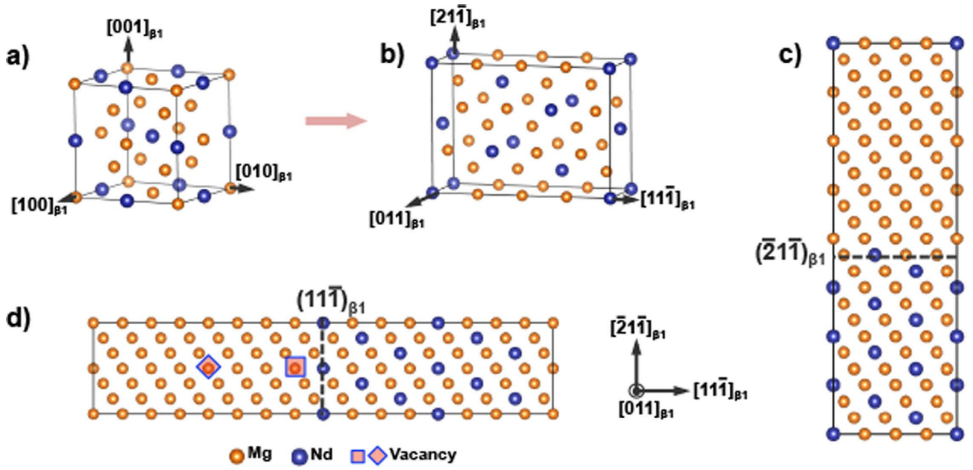

Figure 1. Crystal structures of (**a**) cubic β_1 and (**b**) β_1 in an orthorhombic cell. Pre-relaxed supercells extended along: (**c**) $\langle 112\rangle_{\beta 1}$ and without any prior vacancies, and (**d**) $\langle 111\rangle_{\beta 1}$ and showing the locations of vacancy placed within the "bcc" Mg-region.

Quantitative understanding of β_1/Mg interfaces is crucial for three reasons. First, atomic resolution transmission electron microscopy (TEM) studies have shown that the$\{112\}_{\beta 1}/\{\bar{1}100\}_{Mg}$ interfaces form both longer and shorter edges of β_1 plates[11]. This is surprising. One would have expected at least an additional $\{111\}_{\beta 1}/\{11\bar{2}0\}_{Mg}$ interface, because both $\{112\}_{\beta 1}$ and $\{111\}_{\beta 1}$ planes take part in forming the *hcp*-Mg/β_1 orientation relationship. Second, a well-developed β_1 plate shares a substantial interfacial-area with the parent Mg-matrix. Thus the interfacial energy, in conjunction with transformation strain energy, will likely determine the plate-like morphology[12–15]. Therefore, determination of *hcp*-Mg/β_1 interfacial energies will provide valuable inputs to refine phase field models[12–15]. Third, this study allows us to rationalize whether these coherent interfaces have lower excess energies[16].

Density functional theory (DFT)-based first principles calculations have been used in the past to determine interfacial energies of coherent precipitates in Mg-RE alloys[14,15,17]. So far, DFT studies on Mg-Nd have largely examined the stability of the β'' (ordered *hcp* structure[5]) and the β' precipitate phases[15,17]; both precipitate phases form at early stages prior to β_1 precipitation. For example, Issa *et al.* reported that β'' have positive and negative interfacial energies, when it joins with basal $\{0001\}_{Mg}$ and prismatic $\{\bar{1}100\}_{Mg}$ planes respectively[15,17]. Based on these interfacial energy calculations they proposed that β'' is unstable in Mg-Nd[17], which was later corroborated with TEM observations[18]. The good agreement with experiments validates the available RE pseudopotentials with frozen-core f-electrons, and permits us to study other systems. However, the methodology used for determining negative interfacial energies needs further investigation because one intuitively associates an interface with positive excess energy. Therefore, the rationale for predicted negative interfacial energy was also investigated from the perspective of β_1/Mg interfaces, especially since β_1 is a key-strengthening phase in many commercial alloys[17].

Previous DFT studies on Mg-Nd have not investigated β_1 formation, its interfacial structure, and the associated bonding environment[14,15,17]. Furthermore, they did not examine thermodynamic quantities like surface excess energies - a difficult quantity to measure experimentally in the larger system limit[14,15,17]. Thus, guided by TEM studies[5–11], we have investigated the energetics and structure of two types of β_1/Mg interfaces, namely $\{112\}_{\beta 1}/\{\bar{1}100\}_{Mg}$ and $\{111\}_{\beta 1}/\{11\bar{2}0\}_{Mg}$, via DFT calculations.

Computational Methodology

First principles computations were carried out with the Vienna Ab-initio Simulation Package (VASP) employing the projector-augmented plane-wave (PAW) method[18], with electron exchange and correlation described by the generalized gradient approximation (GGA)[19,20]. All calculations were performed at 0 K, with a cut-off energy of 360 eV, k-point spacing of 0.1 $Å^{-1}$, 0.2 eV Methfessel-Paxton smearing width and Brillouin zone integration at 10^{-7} eV convergence threshold. Groundstate structures of supercells were obtained by relaxing ionic, shape, and volumetric degrees of freedom till global energy convergence was achieved to within 1 meV/atom, and the Hellmann-Feynman forces on the atoms were less than 1 meV/Å. Visualization and subsequent analysis of the relaxed structures was performed using Vesta[21] and Ovito[22].

Results

Construction of initial supercells. Figure 1a shows β_1 Mg3Nd with a BiF_3 structure, lattice parameter 7.391 Å, space group $Fm\bar{3}m$ (#226, similar to *fcc* structures), and Pearson symbol cF16 (corresponding to *bcc*-ordered $D0_3$ *strukturbericht*)[23]. We constructed an orthorhombic β_1 supercell whose edges are parallel to $\langle 011\rangle_{\beta 1}$, $\langle 111\rangle_{\beta 1}$ and $\langle 112\rangle_{\beta 1}$. This choice corresponds to β_1 - *hcp*-Mg orientation relationship seen in experiments[5–11]. Two orthogonal supercells containing 96 atoms, and lengths 35 (Fig. 1c) and 50 Å (Fig. 1d) were used in our analysis. In the resulting supercells (shown in Fig. 1c and d) 12 Nd atoms were replaced with Mg in one portion to create a "Mg-slab", while retaining enough Nd atoms in the remainder to maintain Mg_3Nd stoichiometry corresponding

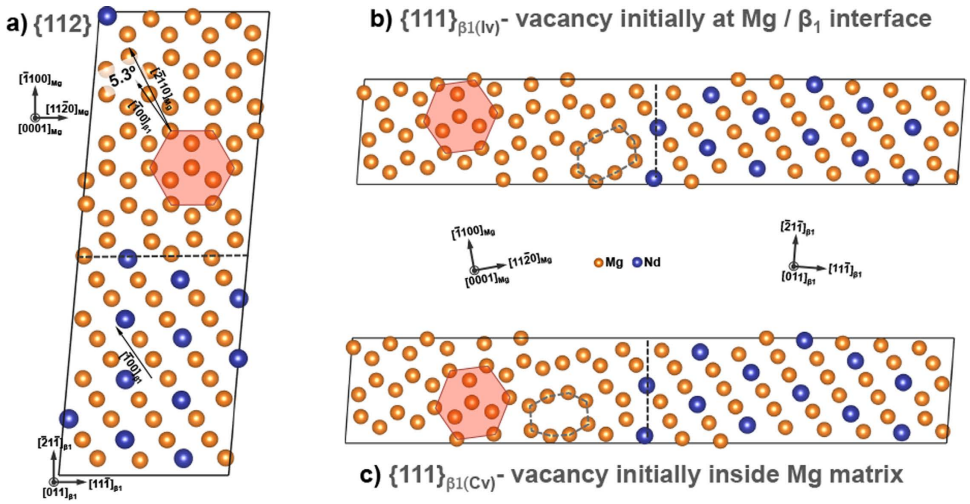

Figure 2. Relaxed supercells showing β_1/Mg interfaces. (**a**) $\{112\}_{\beta1}/\{\bar{1}100\}_{Mg}$ interface, (**b**) $\{111\}_{\beta1(Iv)}/\{11\bar{2}0\}_{Mg}$ interface, with a vacancy that was initially placed near the interface, and (**c**) $\{111\}_{\beta1(Cv)}/\{11\bar{2}0\}_{Mg}$ interface with a vacancy was initially placed at the center of Mg-region.

to β_1. The resulting structures created $\{112\}_{\beta1}$ (hereafter referred to as "{112}" supercell) and $\{111\}_{\beta1}$ interfaces between Mg and the β_1 precipitate as shown in Fig. 1c and d respectively. Note that in these initial supercells, Mg matrix has a "*bcc*" structure.

The Mg-slab was further modified based on the β_1/Mg interfacial structure proposed by Nie and Muddle[5]. They suggested that β_1 formation is associated with vacancies near the β_1/Mg interface along $\langle 111\rangle_{\beta1}$ [5]. Concomitantly, recent analytical calculations, involving stress-free transformations strains during β_1 formation[11,13], indicated the presence of a tensile strain along $\langle 111\rangle_{\beta1}$. Such tensile strains likely facilitate vacancy creation along $\langle 111\rangle_{\beta1}$ by expanding the volume near the interfaces. Therefore, to understand such effects a Mg vacancy was introduced near the β_1/Mg interface (square, Fig. 1d) and at the center of Mg (diamond, Fig. 1d) in separate supercells. An Mg vacancy is placed inside "Mg" slab, rather than in the intermetallic β_1 compound, was guided by β_1/Mg interfacial structure proposed in literature[6,11]. Also, this reasonable because Mg vacancy formation energies in β_1 (1.24 eV) is greater than in *hcp*-Mg (0.82 eV). The resulting vacancy concentration was ~1 at% for the entire supercell, and 2at% for the Mg slab. Hereon the vacancy containing supercells - near β_1/Mg interface, and center of Mg slab - will be referred to as "$\{111\}_{\beta1(Iv)}$" and "$\{111\}_{\beta1(Cv)}$" supercells respectively.

Relaxed structures. The relaxed structures of three supercells with β_1/Mg interfaces are shown in Fig. 2. In the {112}, $\{111\}_{\beta1(Iv)}$ and $\{111\}_{\beta1(Cv)}$ supercells (Figs 1a and 2b,c respectively), the Mg slab with an initial *bcc* structure transforms to the correct *hcp* crystal structure indicated by hexagons in Fig. 2. The β_1 however, retains its *bcc*-ordered structure as confirmed by common neighbor analysis (CNA)[22,24]. In this manner we created "equilibrium" supercells comprising of two types of β_1/*hcp*-Mg interfaces: $\{112\}_{\beta1}//\{\bar{1}100\}_{Mg}$ and $\{111\}_{\beta1(Iv/Cv)}//\{11\bar{2}0\}_{Mg}$. The structural relaxation of $\{111\}_{\beta1(Iv)}$ and $\{111\}_{\beta1(Cv)}$ supercells (Fig. 2b and c), with an added vacancy (Fig. 1d), also created a region with vacancy-like excess free volume marked by dotted polygons in Fig. 2b and c. This occurs even when a single vacancy was initially placed at the center of the Mg slab (Fig. 1d). The excess volume of *hcp*-Mg in Fig. 2b and c measured by Voronoi tessellation[21], was ~30 Å^3, and ~23 Å^3. In comparison, Mg slabs without prior vacancies inside the {111} supercell, did not have an excess volume regions and neither did their initial *bcc* Mg relax to a *hcp* structure (Supplementary Figure S1) – unlike those presented in Fig. 2b and c. Thus vacancies aid in the transformation of *bcc*-Mg to *hcp*.

In the relaxed {112} supercell, Fig. 2a, certain crystallographic orientations of Mg and β_1 were mutually coincident and exhibited the following orientation relationship (OR): $(0001)_{Mg}//(011)_{\beta1}$, $[\bar{1}100]_{Mg}//[21\bar{1}]_{\beta1}$, and $[11\bar{2}0]_{Mg}//[1\bar{1}1]_{\beta1}$. Electron diffraction patterns from literature have indicated that the β_1-Mg OR causes a ~5.26° misorientation between $(0001)_{Mg}$ and $(011)_{\beta1}$ planes[5–11], which is in excellent agreement with DFT value of 5.3° indicated in Fig. 2a, and, also validates our approach. The misorientation can be quantified as the angle between $[1\bar{1}00]_{\beta1}$ and $[\bar{2}110]_{Mg}$.

A comparison of β_1 and Mg crystallographic directions within $\{111\}_{\beta1(Iv)}$ and $\{111\}_{\beta1(Cv)}$ supercells showed that, eventhough $(0001)_{Mg}$ and $(011)_{\beta1}$ planes are parallel, the other crystallographic axes involved in β_1-Mg OR are not coincident. For example, angle between $[\bar{1}100]_{Mg}$ and $[21\bar{1}]_{\beta1}$ in $\{111\}_{Iv}$ and $\{111\}_{Cv}$ is ~15°, while those axes are coincident in case of the {112} supercell. In other words, DFT calculations suggest that a creation of only $\{111\}_{\beta1(Iv/Cv)}/\{11\bar{2}0\}_{Mg}$ interfaces may not yield the experimentally seen β_1-Mg OR atleast near the interfacial regions. This result is surprising because, based on the β_1-Mg orientation relationship, one would have expected a mutual alignment of β_1 and Mg orientations in the $\{111\}_{\beta1(Iv/C/v)}$ supercells.

Implication of this "off β_1-Mg OR" misalignment in the $\{111\}_{\beta1(Iv/C/v)}$ supercells was further probed by comparing it's local atomic distortions with the {112} supercells. Mg-Mg, Mg-Nd and Nd-Nd bond-lengths measured from regions 3–4 atomic layers away from the interfaces were used to calculate the lattice strain

Interface	Mg matrix		β_1 precipitate a (Å)/strain (%)
	a (Å)/strain (%)	c(Å)/strain (%)	
$\{211\}_{\beta1}/\{0110\}_{Mg}$ – No vacancy	3.186/−0.28	5.206/+0.51	7.385/− 0.37
$\{111\}_{\beta1}/\{1120\}_{Mg}$ – Vacancy initially at the interface	3.282/+2.73	5.202/+0.43	7.282/−1.76
$\{111\}_{\beta1}/\{1120\}_{Mg}$ – Vacancy initially inside Mg	3.276/+2.53	5.220/+0.78	7.239/−2.34

Table 1. Table of lattice parameters and strain in Mg and β_1 slabs of the relaxed structures. Calculated lattice parameters of bulk phases: Mg − 3.195 Å and 5.180 Å and β_1 − 7.412 Å.

$\epsilon = \left[(a_{\beta1/Mg-interface} - a_{bulk})/a_{bulk}\right] * 100$, where $a_{\beta1/Mg\text{-}interface}$ and a_{bulk} are the lattice parameters of each phase in the supercells, and their bulk equilibrium lattice respectively. Table 1 lists the β_1 and Mg lattice parameters, and the lattice strains. Lattice strains, 5–10 times larger that the bulk systems, were found in $\{111\}_{\beta1(Iv)}$ and $\{111\}_{\beta1(Cv)}$ supercells along the a-axis of Mg or $\langle 11\bar{2}0\rangle$ and $\langle 100\rangle$ of β_1. We further note that placement of vacancy away from $\{111\}_{\beta1(Iv)}/\{11\bar{2}0\}_{Mg}$ interface (Fig. 1d) increases the β_1 lattice strain by ~33% in $\{111\}_{\beta1(Cv)}$ in comparison to $\{111\}_{\beta1(Iv)}$. In other words, higher lattice strains are associated with the formation of $\{111\}_{\beta1}/\{11\bar{2}0\}_{Mg}$ interfaces than $\{112\}_{\beta1}/\{01\bar{1}0\}_{Mg}$. Regardless, presence of vacancy-like excess volume in the $\{111\}_{\beta1(Iv/Cv)}$ supercells strains the Mg and β_1 lattice, and will be shown to affect the β_1/Mg interfacial energies.

β_1/Mg interfacial energies. The geometry used for calculating β_1/Mg interfacial energies ($\gamma_{\beta1/Mg}$) is schematically shown in Fig. 3a as vacuum-space/bulk-β_1/bulk-Mg/vacuum-space. Here the interacting β_1/Mg surfaces are $\{111\}_{\beta1(Iv/Cv)}/\{11\bar{2}0\}_{Mg}$ and $\{112\}_{\beta1}/\{01\bar{1}0\}_{Mg}$ (see Supplementary Figure 2). This methodology was previously used by Liu *et al.* to examine the interface between an ordered intermetallic compound and the disordered matrix[25]. This approach further avoids the development of excess artificial interfacial strains by having vacuum on both sides of the unconstrained interfacial supercell. Thus, one need not include additional coherency strain energy terms (e.g. ref. 17) to evaluate the interfacial energies. Furthermore, since β_1 and Mg are exposed to the vacuum on either ends (Fig. 3a), we are required to determine the "free" surface of the participating $\{111\}_{\beta1,}$ $\{11\bar{2}0\}_{Mg}$, $\{112\}_{\beta1}$ and $\{\bar{1}100\}_{Mg}$ planes. The free surface energy, $\gamma_{S\text{-}p}$, for a phase "p" was calculated using the expression $\gamma_{S-p} = [E_p(N) - N * E_{Bulk-p}]/2A$, where $E_p(N)$ is the calculated ground state energy for a "N" atomic layer supercell slab of phase "p", $E_{Bulk\text{-}P}$ is the bulk energy of phase "p", and A is the surface area[25–27]. The calculations involved a maximum of 24 (~35 Å) and 60 (~50 Å) layers for Mg and β_1 respectively, and a minimum of ~12 Å of vacuum space. $E_{Bulk\text{-}P}$ was determined from the slope of $E_p(N)$ vs N plot. For pure metals, $E_{Bulk\text{-}P}$ corresponds to their cohesive energy[27], and our calculations yielded 1.53 eV/atom for Mg - in excellent agreement with literature[26–28]. Figure 3b shows that plot of $\gamma_{S\text{-}p}$ vs. N for different β_1 and Mg planes, and the results indicated that the $\gamma_{S\text{-}p}$ values, for $\{111\}_{\beta1(Iv/Cv),}$ $\{11\bar{2}0\}_{Mg}$, $\{112\}_{\beta1}$ and $\{\bar{1}100\}_{Mg}$ planes rapidly converge within the chosen range of N.

The $\gamma_{S\text{-}p}$ values for the Mg and β_1 planes were calculated using linear fits ($R^2 \approx 0.94$) to $\gamma_{S\text{-}p}$ vs. 1/N plots (Fig. 3c). We then extrapolated the fits for $1/N \rightarrow 0$, which correspond to $N \rightarrow \infty$ layers or the "bulk". Our surface energy $\gamma_{S\text{-}p}$ of $(0001)_{Mg}$ was 0.52 J/m^2, agreed well with literature reports of 0.52 and 0.55 J/m^2 [26,27]. Figure 3b shows that β_1 has higher excess surface energies ($\gamma_{S\text{-}p}$) than pure Mg. This indicates a stronger bonding within β_1, and that it is difficult to cleave or fracture β_1 during deformation. We further note that such surface excess energies have not been reported for any other precipitate phases in Mg-RE systems[14–16].

The plots in Fig. 3b and c helps estimate the optimal value of "N" required for the interfacial energy calculations that reasonably accounts for the bulk phases along with the free-surface and interfacial energies. Thus, 12 (~15 Å) and 24 (~25 Å) layers was chosen for each phase making up the $\{112\}_{\beta1}/\{\bar{1}100\}_{Mg}$ and $\{111\}_{\beta1}/\{11\bar{2}0\}_{Mg}$ interfaces respectively, and ~12 Å of vacuum was maintained above β_1 and Mg slabs (Fig. 3a). β_1/Mg interfacial energy ($\gamma_{\beta1/Mg}$) was estimated using the expression[22]:

$$\gamma_{\beta1/Mg} = \left(E_{supercell} - E_{Bulk-\beta1} - E_{Bulk-Mg}\right)/A - (\gamma_{S-\beta1} + \gamma_{S-Mg}) \quad (1)$$

where $\gamma_{S\text{-}\beta1}$ and $\gamma_{S\text{-}Mg}$ are the free surface energies of β_1 and Mg respectively, $E_{supercell}$ is the ground state energy of the β_1-Mg supercell while $E_{Bulk\text{-}\beta1}$ and $E_{Bulk\text{-}Mg}$ are the bulk energies of β_1 and Mg respectively, and A is the surface area. The $\gamma_{\beta1/Mg}$ values of these three interfaces are plotted in Fig. 3d as a bar chart. Their respective relaxed structures are also shown in Supplementary Figure 2. The calculated $\gamma_{\beta1/Mg}$ values for $\{112\}_{\beta1}$, $\{111\}_{\beta1(Cv)}$ and $\{111\}_{\beta1(Iv)}$ supercells were 98, 282 and 762 mJ/m^2 respectively. Thus, the $\{112\}_{\beta1}/\{\bar{1}100\}_{Mg}$ interfaces are more energetically stable than $\{111\}_{\beta1}/\{11\bar{2}0\}_{Mg}$. Also note that inclusion of excess surfaces energies for estimating interfacial energies (equation 1) will result in only positive excess energy values, which is thermodynamically reasonable.

Structure and bonding environment near β_1/Mg interfaces. To explain the lower interfacial energy of $\{112\}_{\beta1}/\{\bar{1}100\}_{Mg}$ in Fig. 3d, we have compared the bonding environment of these interfaces. The analysis correlates the interfacial atomic-coordination (Fig. 4a and c), with electron charge density distribution (Fig. 4b and d).

In Fig. 4a and c the atom colors are assigned by CNA environment type[18,20] and the bonds depict in-plane – i.e. $(0001)_{Mg}//(011)_{\beta1}$ – coordination around an atomic site: (i) red denotes *hcp*-Mg with 6 in-plane coordination, (ii) blue denotes *bcc*-ordered β_1 with 4 in-plane coordination, and (iii) green depicts sites which were not identified as either *hcp*-Mg or β_1. Thus, the green-colored bonds/atoms near the interfacial regions - indicated with

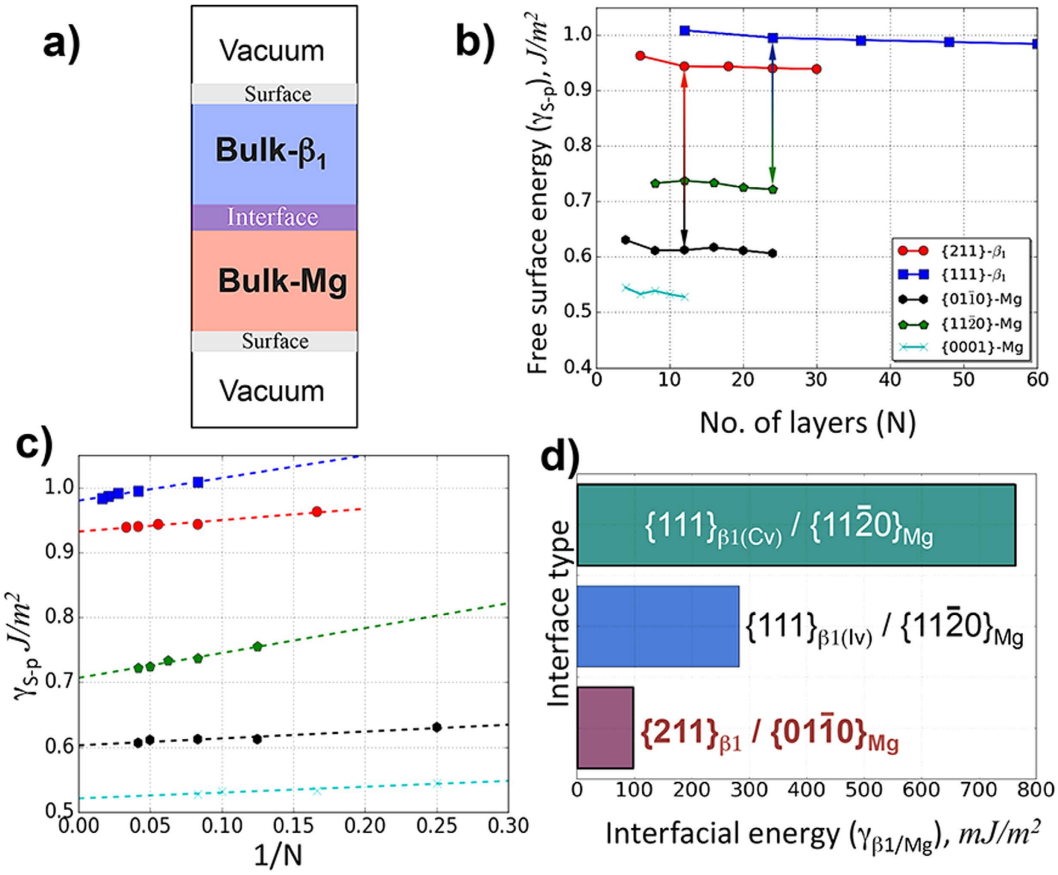

Figure 3. (**a**) Configuration used for calculating β_1/*hcp*-Mg interfacial energy. (**b**) Free surface energies ($\gamma_{S\text{-}p}$) of different β_1 and Mg surface planes plotted as a function of number of atomic layers (N). (**c**) $\gamma_{S\text{-}p}$ vs 1/N plots to determine $\gamma_{S\text{-}p}$ in the larger size limit. The dotted line fits corresponding to R^2 values of 0.94. The intercept of the linear fits, $1/N \rightarrow 0$ yield excess surface energy in the large system limit ($N \rightarrow \infty$), which is a well-defined thermodynamic quantity. (**d**) Bar chart showing the interfacial energies of three β_1/Mg interfaces reveal $\{112\}_{\beta1}/\{\bar{1}100\}_{Mg}$ interfaces are energetically more stable than $\{111\}_{\beta1}/\{11\bar{2}0\}_{Mg}$.

shaded boxes across Fig. 4a–d - can be interpreted as distortion of the lattice sites, from bulk *hcp*-Mg and β_1 structures.

A comparison of the interfacial regions, and their corresponding bonding environment reveal that the distorted lattice sites (shown by green colored bonds) are invariably located around regions with significant depletion of electron charge density distributions (marked by red arrows in Fig. 4b and d). In other words, interfacial lattice distortions correlate well with lower electron density or weak bonding[29]. Furthermore, the electron density distributions near the interfacial regions of $\{111\}_{\beta1(Iv)}/\{11\bar{2}0\}_{Mg}$ was discernibly lower (compare Fig. 4b and c with legend at the bottom), and spread over a wider region than $\{112\}_{\beta1}/\{\bar{1}100\}_{Mg}$. Correspondingly, lattice significantly distorted near the $\{111\}_{\beta1(Iv)}/\{11\bar{2}0\}_{Mg}$ interface. Therefore, considering the larger differences in the energies of $\{112\}_{\beta1}/\{\bar{1}100\}_{Mg}$ (98 mJ/m^2) and $\{111\}_{\beta1(Iv)}/\{11\bar{2}0\}_{Mg}$ (282 mJ/m^2) interfaces, it is evident that smaller population of distorted lattice sites and narrow spatial extent near the interface correlate with lower interfacial energy. This is further confirmed for $\{111\}_{\beta1(Cv)}/\{11\bar{2}0\}_{Mg}$ system (762 mJ/m^2) in Fig. 4e, which displayed a wider spatial extent of distorted interfacial lattice sites (overlapping both *hcp*-Mg and β_1 structures) than the other two interfaces.

Discussion

One of our motivations was to rationalize the existence of only $\{112\}_{\beta1}/\{\bar{1}100\}_{Mg}$ interfaces seen in Mg-Nd alloys, which was contrary to the exceptions based on β_1/Mg OR[11]. The DFT calculations revealed that, unlike $\{112\}_{\beta1}/\{\bar{1}100\}_{Mg}$, formation of $\{111\}_{\beta1}/\{11\bar{2}0\}_{Mg}$ requires the presence of vacancy-like excess volume near the interfaces, which causes interfacial distortions, higher lattice strains and presumably strain energy within the mating phases. Such pronounced distortion/strain increases the interatomic spacings near the interface, reduces charge density between the atoms, and creates weaker interfacial bonding in $\{111\}_{\beta1}/\{11\bar{2}0\}_{Mg}$. The relatively poor bonding increases the excess energy of $\{111\}_{\beta1}/\{11\bar{2}0\}_{Mg}$ incomparison to the $\{112\}_{\beta1}/\{\bar{1}100\}_{Mg}$ interface, and makes the latter an energetically preferable interface."

Despite the fact that excess volume results in an energetically unstable $\{111\}_{\beta1}/\{11\bar{2}0\}_{Mg}$ interface. However, the presence of such excess volume near the interfaces may explain the growth of plate-like β_1 within Mg-matrix and along dislocation lines[5–11]. Nie and Muddle have proposed that shear transformation strains are associated with

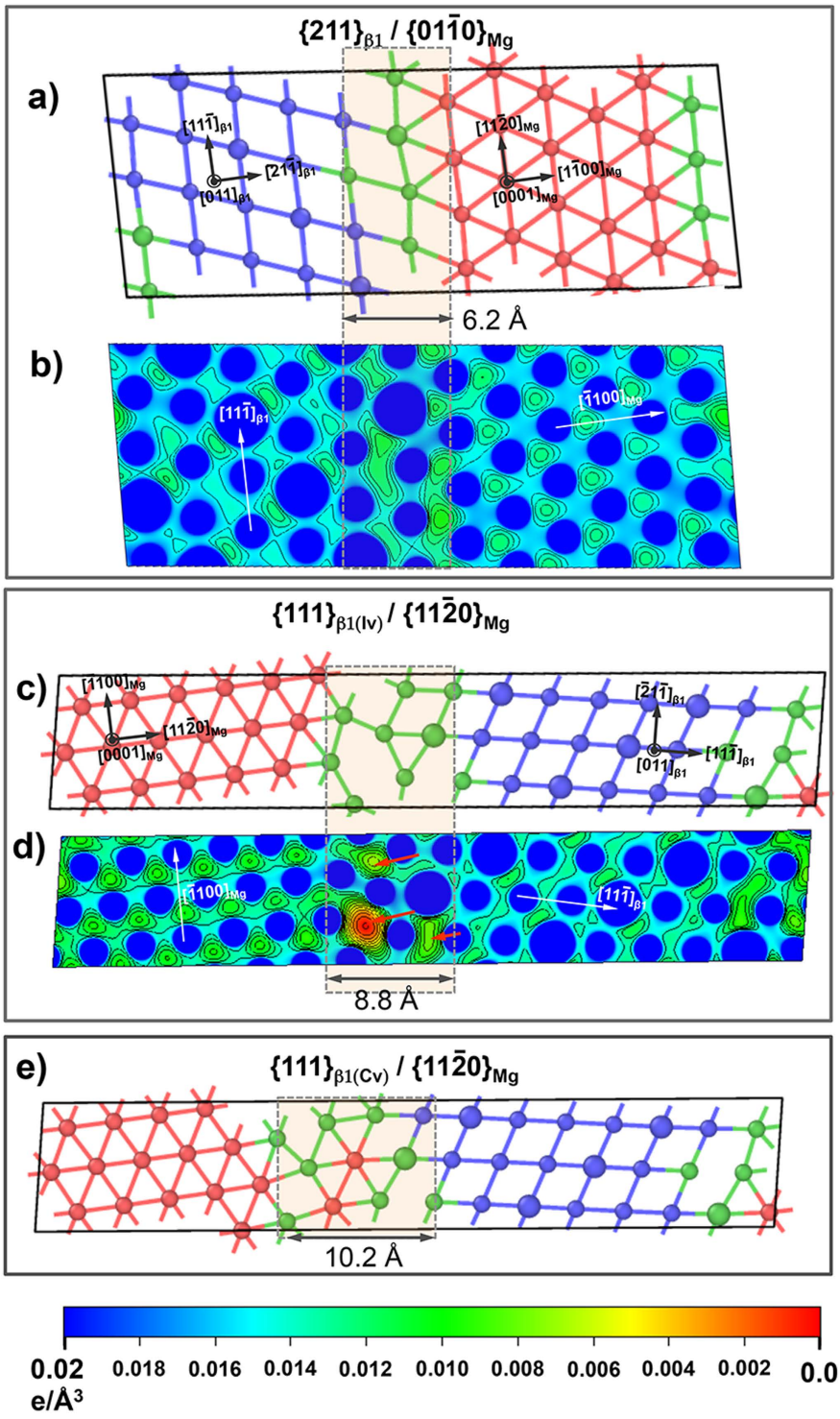

Figure 4. (**a,b**) and (**c,d**) show structure and electron charge distributions of $\{112\}_{\beta1}/\{\bar{1}100\}_{Mg}$ and $\{111\}_{\beta1(Iv)}/\{11\bar{2}0\}_{Mg}$ interfaces respectively. In (**a**) and (**b**) red and blue colors indicate atomic sites in *hcp*-Mg and β_1 structures respectively, while green indicates "distorted" lattice sites. (**e**) shows the legend for electron charge densities in (**b**) and (**d**). (**e**) shows the structure of $\{111\}_{\beta1(Cv)}/\{11\bar{2}0\}_{Mg}$ interface. Interfacial width is indicated by translucent boxes, and the contours in the electron charge density plots engulf regions with lower charge densities compared to the bulk.

β_1 formation, because of which excess vacancy concentration is created at the short ends oriented along $\langle 11\bar{2}0\rangle_{Mg}$. It is likely β_1 growth can occur via vacancy migration to the interfaces. However, to maintain elongated plate-like morphology during the growth process, β_1 needs a stable interface in its long edge. Our DFT results suggest that

a low lattice strain and interfacial energy of $\{112\}_{\beta 1}/\{100\}_{Mg}$ interfaces allows β_1 precipitates to acquire a plate-like morphology with a high aspect ratio and possess a broad $\{112\}_{\beta 1}$-face parallel to $\{1\bar{1}00\}_{Mg}$ as seen in experiments[4–12]. In the case of dislocation assisted β_1 form as linear chains along $\langle 11\bar{2}0\rangle_{Mg}$ [10,13,30], which are also observed in our creep-tested microstructures[10]. We postulate that such linear growth of β_1 along dislocation lines occur via transfer of vacancies to metastable interfaces like $\{111\}_{\beta 1(Iv)}/\{11\bar{2}0\}_{Mg}$ (Fig. 2b), which tends to have lower interfacial energy than vacancy formation away form the β_1/Mg interface (i.e. $\{111\}_{\beta 1(Cv)}/\{11\bar{2}0\}_{Mg}$ in Figs 2c and 3d). Since dislocations can rapidly supply vacancies via dislocation pipe diffusion, the diffusion assisted movement of $\{111\}_{\beta 1(Iv)}/\{11\bar{2}0\}_{Mg}$ type interfaces rapidly consumes a large portion of the host dislocation line, and orients β_1 along $\langle 11\bar{2}0\rangle_{Mg}$. Finally, since $\{111\}_{\beta 1(Iv)}/\{11\bar{2}0\}_{Mg}$ interfaces are energetically unfavorable, interfacial atomic rearrangements, e.g. via shear process[5,6], produces $\{112\}_{\beta 1}/\{\bar{1}100\}_{Mg}$ interfaces in the final microstructure.

From the perspective of alloy design approaches; the contribution of this report is two fold. We demonstrate that in order to develop alloys with advantages associated with "β_1-like" precipitation one needs to (i) retain a well bonded coherent interface at the precipitate broad faces, e.g. $\{112\}_{\beta 1}/\{\bar{1}100\}_{Mg}$, while simultaneously (ii) form mobile yet unstable interfaces on the short edges to allow precipitate growth along dislocation lines. However, finding non-RE substitutions, which fits these two criteria, is our next challenge, and is currently being tackled by coupling evolutionary algorithms with first principle calculations.

Conclusion

Formation of nanoscale β_1-Mg_3Nd precipitates in *hcp*-Mg matrix is known to enhance the creep resistance of Mg-alloys because of their tendency to form on dislocation lines and sluggish coarsening kinetics when they form in the *hcp* alloy matrix. Using first principles calculations, we have compared the excess energy and the structure of $\{112\}_{\beta 1}/\{\bar{1}100\}_{Mg}$ and $\{111\}_{\beta 1}/\{11\bar{2}0\}_{Mg}$ interfaces. Our calculations revealed that the formation of $\{112\}_{\beta 1}/\{\bar{1}100\}_{Mg}$ interfaces, compared to $\{111\}_{\beta 1}/\{11\bar{2}0\}_{Mg}$ interface, is associated with significant reduction in both the interfacial energy and lattice strains in the adjacent β_1 and Mg matrix. The favorable formation energetics of the $\{112\}_{\beta 1}/\{\bar{1}100\}_{Mg}$ interface, in conjunction with small lattice strains, influences β_1 acquiring a plate-like morphology with its broad-face $\{112\}_{\beta 1}$ parallel to $\{\bar{1}100\}_{Mg}$. Electronic structure of these interfaces revealed that a lower interfacial energy also correlates with a smaller population of distorted lattice sites near the interfacial regions. Additionally, our DFT investigation informs that creep-resistant Mg alloys will benefit from "β_1-like" precipitation because of two key features (i) retain a well bonded coherent interface at the precipitate broad faces, e.g. $\{112\}_{\beta 1}/\{\bar{1}100\}_{Mg}$, and (ii) destabilize other interfaces (corresponding to precipitate-Mg OR) to promote growth along a desired direction, e.g $\langle 11\bar{2}0\rangle_{Mg}$.

References

1. Luo, A. & Pekguleryuz, M. O. Cast magnesium alloys for elevated temperature applications. *J. Mater. Sci.* **29,** 5259–5271 (1994).
2. Mordike, B. L. Creep-resistant magnesium alloys. *Mater. Sci. Eng A*. **A324,** 103–112 (2002).
3. Vagarli, S. S. & Langdon, T. G. Deformation mechanism in H.C.P. metals at elevated temperatures – I. Creep behavior of magnesium. *Acta Metall.* **29,** 1969–1982 (1981).
4. Vagarli, S. S. & Langdon, T. G. Deformation mechanism in H.C.P. metals at elevated temperatures – II. Creep behavior of Mg-0.8%Al solid solution alloy. *Acta Metall.* **30,** 1157–1170 (1982).
5. Nie, J. F. Precipitation and hardening in magnesium alloys. *Metall. Mater. Trans. A.* **43,** 3891–3939 (2012).
6. Nie, J. F. & Muddle, B. C. Characterization of strengthening precipitate phases in a Mg–Y–Nd alloy. *Acta. Mater.* **48,** 1691–1703 (2000).
7. Saito, K. & Kenji, H. The structures of precipitates in an Mg-0.5 at% Nd age-hardened alloy studied by HAADF-STEM technique. *Mater. Trans.* **52,** 1860–1867 (2011).
8. Choudhuri, D. *et al.* Evolution of a honeycomb network of precipitates in a hot-rolled commercial Mg–Y–Nd–Zr alloy. *Phil. Mag. Lett.* **93,** 395–404 (2013).
9. Zhu, S. M., Gibson, M. A., Easton, M. A. & Nie, J. F. The relationship between microstructure and creep resistance in die-cast magnesium–rare earth alloys. *Scripta Mater.* **63,** 698–703 (2010).
10. Choudhuri, D. *et al.* Homogeneous and heterogeneous precipitation mechanisms in a binary Mg–Nd alloy. *J. Mater. Sci.* **49,** 6986–7003 (2014).
11. Zhou, X., Weyland, M. & Nie, J. F. On the strain accommodation of β_1 precipitates in magnesium alloy WE54. *Acta Mater.* **75,** 122–133 (2014).
12. Gao, Y. *et al.* Simulation study of precipitation in an Mg–Y–Nd alloy. *Acta Mater.* **60,** 4819–4832 (2012).
13. Liu, H. *et al.* A simulation study of $\beta 1$ precipitation on dislocations in an Mg–rare earth alloy. *Acta Mater.* **77,** 133–150 (2014).
14. Liu, H., *et al.* A simulation study of the shape of β' precipitates in Mg–Y and Mg–Gd alloys. *Acta Mater.* **61,** 453–4662 (2013).
15. Ji, Y. Z. *et al.* Predicting β' precipitate morphology and evolution in Mg–RE alloys using a combination of first-principles calculations and phase-field modeling. *Acta Materi*. **76,** 259–271 (2014).
16. Sutton, A. P. & Balluffi, R. W. Overview no. 61 On geometric criteria for low interfacial energy. *Acta Metall*., **35,** 2177–2201 (1987).
17. Issa, A., Saal, J. E. & Wolverton C. Formation of high-strength β' precipitates in Mg–RE alloys: The role of the Mg/β precipitate instability. *Acta Mater.* **83,** 75–83 (2015).
18. Nie, J. F., Wilson, N. C., Zhu, Y. M. & Xu, Z. Solute clusters and GP zones in binary Mg–RE alloys. *Acta Mater.* **106,** 260–271 (2016).
19. Kresse, G. & Hafner J. Ab inito molecular dynamics for metals. *Phys. Rev. B.* **47,** 558–561 (1993).
20. Perdew, J. P., Kieron, B. & Ernzerhof, M. Generalized gradient approximation made simple. *Phys. Rev. Lett.* **77,** 3865–3868 (1996).
21. Koichi, M. & Izumi, F. VESTA: a three-dimensional visualization system for electronic and structural analysis. *J. Appl. Cryst.* **41,** 653–658 (2008).
22. Stukowski, A. Visualization and analysis of atomistic simulation data with OVITO–the Open Visualization Tool. *Modelling Simul. Mater. Sci. Eng.* **18,** 015012 (2009).
23. Villaes, P. & Calvent L. D. Person's Handbook of Crystallographic Data for Intermetallic phases, vol. 23. *The Materials Information Society*. 2691 (1996).
24. Stukowski, A. Structure identification methods for atomistic simulations of crystalline materials. *Modelling Simul. Mater. Sci. Eng.* **20,** 045021 (2012).
25. Liu, W., Li, J. C., Zheng, W. T. & Jiang, Q. Ni Al (110)/Cr (110) interface: A density functional theory study. *Phys. Rev. B.* **73,** 205421 (2006).

26. Wachowicz, E. & Kiejna, A. Bulk and surface properties of hexagonal-close-packed Be and Mg. *J. Phys. Condens. Matter*. **13,** 10767 (2001).
27. Markus, J. & Groß, A. Microscopic properties of lithium, sodium, and magnesium battery anode materials related to possible dendrite growth. *J. Chem. Phys.* **141,** 174710 (2014).
28. Kittel, C. *Introduction to Solid State Physics*, 8th ed. (John Wiley & Sons, New York, 2004).
29. Sutton, Adrian P. *Electronic structure of materials*. (Clarendon Press, pp-29 1993).
30. Zhu, Y. M., Liu, H., XuZ., Wang, Y. & Nie, J. F. Linear-chain configuration of precipitates in Mg–Nd alloys. *Acta Mater.* **83,** 239–247 (2015).

Acknowledgements

The authors used UNT's Talon2 High Performance Computing cluster, and Texas Advance Computing Center's Stampede. D.C., R.B. and S.G.S. also acknowledge support from grant# NSF-DMR-1435611.

Author Contributions

D.C., S.G.S., and R.B. conceptualized this work. D.C. ran the simulations. All authors contributed in writing this manuscript.

Additional Information

Supplementary information accompanies this paper at http://www.nature.com/srep

Competing financial interests: The authors declare no competing financial interests.

How to cite this article: Choudhuri, D. *et al.* Interfacial structures and energetics of the strengthening precipitate phase in creep-resistant Mg-Nd-based alloys. *Sci. Rep.* **7**, 40540; doi: 10.1038/srep40540 (2017).

Publisher's note: Springer Nature remains neutral with regard to jurisdictional claims in published maps and institutional affiliations.